Fourth International Symposium on Marine Propulsors
smp'15, Austin, Texas, USA, June 2015

Use of Acoustic Analogy for Marine Propeller Noise Characterisation

Artur K. Lidtke[1], Stephen R. Turnock[1], Victor F. Humphrey[2]

[1] *Fluid Structure Interactions Research Group, University of Southampton, Southampton, SO17 2BJ, UK*
[2] *Institute of Sound and Vibration Research, University of Southampton, Southampton, SO17 2BJ, UK*

ABSTRACT

Being able to predict shipborne noise is of significant importance to international maritime community. Porous Ffowcs-Williams Hawkings acoustic analogy is used with cavitation model by Sauer & Schnerr in order to predict the noise signature of the Potsdam Propeller operating in open water. The radiation pattern is shown to be predominantly affected by a dipole source, in addition to less prominent sources at the propeller plane and in the wake. It is shown that the predicted sound pressure levels depend on the choice of the control surface and grid density. The unsteady RANS method is shown to be capable of capturing the blade harmonic noise components but lacks the ability to deal with the broadband part of the noise spectrum, both cavitation and turbulence induced, if no additional modelling is used.

Keywords

Cavitation, Noise, Hydroacoustics, Acoustic Analogy.

1 INTRODUCTION

Input of anthropogenic noise into the Oceans has raised significant concerns in recent years, stimulating discussion about introducing potential regulatory means in the future (Kellet et al. 2014). Shipping, being one of the larger noise sources responsible for this type of marine pollution, typically covers the frequency range between 10 and 1000 Hz and hence may affect marine wildlife (Hilderbrand 2009, Urick 1984, Lloyd 2013).

Specifically, the sound radiated by a ship underway has two primary components: tonal, related to the blade pass frequency, and broadband, associated with the presence of unsteadiness in the flow. These may be categorised into the blade thickness (monopole), blade loading (dipole), and non-linear (quadrupole) terms (Marte & Kurtz 1970). Presence of cavitation also has a significant potential for modifying the noise signature of a marine propeller. This may take several forms, such as bubble, tip or root vortex, sheet, hub, and propeller-hull cavitation (Woo Shin 2010), all of which behave in a distinct manner. The main noise generation mechanisms of cavities are associated with the oscillation of the bubble volumes, or interface velocities, acting similarly to a thickness (monopole) source, and the presence of shockwaves occurring, for instance, during bubble collapse or the passing of a re-entrant jet (Brennen 1993, Seo et al. 2008, Kirsteins et al. 2011, Park et al. 2009, Salvatore & Ianniello 2002).

In order for an acoustic signature of a propeller to be computed directly one must consider the compressible form of the governing flow equations. Doing so may impose significant limitations on the time step due to high speed of sound in water (Wikstrom 2006, Ianiello et al. 2013). One of the alternatives is the use of acoustic analogies, which allow for the radiated noise to be evaluated from the results of an incompressible flow simulation. In particular, the porous method presented by Ffowcs-Williams & Hawkings (1969) is appealing as it allows one to account for the non-linear terms without the need for volume integration, offers short computational times, and does not require the flow solver to be modified. Contrary to a typical acoustic analogy where the noise terms are evaluated on the surface of the body, it does so on a permeable surface surrounding the object and flow features contributing to the radiated noise, such as cavities or wake.

Multiple aeroacoustic studies utilising the Ffowcs-Williams Hawkings (FWH) analogy have been presented in the literature (Brentner & Farassat 1998), which is accompanied by more recent investigations in the hydroacoustic context, such as those performed by Ianiello et al. (2013), Seol et al. (2005), Salvatore & Ianiello (2002), or Lloyd et al. (2014). Most of the authors, however, focus on the influence of either turbulence or cavitation on the radiated noise, while, as discussed by Bensow (2011), the two may be expected to be interdependent in reality, effectively changing the behaviour of the associated noise sources.

Preliminary results are presented in this study where the noise signature of the Potsdam Propeller Test Case (PPTC) in cavitating condition is considered (Abdel-Maksoud 2011). The methodology presented makes use of the mass transfer model by Sauer & Schnerr (2001) and Ffowcs-Williams Hawkings (1969) acoustic analogy implemented in OpenFOAM. At present, turbulence modelling is achieved using the $k-\omega$ SST URANS model which should be capable of capturing the tonal part of the noise.

Focus of the analysis is put on developing first-hand experience with using FWH analogy in application to a marine propeller, studying the effect of choosing different integration surfaces for the porous acoustic formulation, and better understanding the distribution of the individual noise terms inside the control volume. Finally, an assessment is made as to how usable the presented, or similar, method would be in performing design calculations for a newly built ship, should such information be required by the regulatory bodies in the future.

2 FORMULATION

2.1 Cavitation Model

Cavitation is the transition of liquid into vapour in regions of low pressure caused by the presence of small gas nuclei in the fluid (Plesset & Prosperetti 1977). The latter expand, collapse, or oscillate when subject to stress. A fair degree of understanding of the bubble physics allows one to simulate their behaviour, as described, for instance, by Jamaluddin et al. (2011) or Hsiao & Chahine (2004). However, because of the small size of the cavitation nuclei, ranging between 2 and 50 µm for standard sea water (Woo Shin 2010), computing the behaviour of every individual bubble in full detail for a flow over a full-scale propeller or a hydrofoil would be computationally intensive.

Alternative modelling approaches exist where instead of individual bubble physics the large-scale cavities are considered. In the present study the model by Sauer & Schnerr (2001) has been used in order to account for the pressure-induced phase change of liquid into vapour and *vice versa*. In this approach the cavities are described using vapour fraction with both the liquid and vapour phases occupying the same physical space and being governed by the same set of equations of motion.

This is done based on solving the transport equation for a volume fraction, α, with an additional source term introduced on the right-hand side to account for the evaporation and condensation:

$$\frac{\partial \alpha}{\partial t} + \nabla \cdot (\alpha \boldsymbol{U}) = -\frac{\dot{m}}{\rho}. \tag{1}$$

In equation (1) $\dot{m}$ denotes the rate of change of mass of the liquid-vapour mixture, ρ is the density of the mixture and $\boldsymbol{U}$ is the fluid velocity. The presence of the additional source term also modifies the continuity equation which now becomes

$$\nabla \cdot \bar{\boldsymbol{U}} = \left(\frac{1}{\rho_v} - \frac{1}{\rho_l}\right)\dot{m}, \tag{2}$$

where subscripts v and l refer to vapour and liquid phases, respectively.

One may also define the density and viscosity of the liquid-vapour mixture as

$$\begin{aligned} \rho &= \alpha\rho_v + (1-\alpha)\rho_l, \\ \mu &= \alpha\mu_v + (1-\alpha)\mu_l, \end{aligned} \tag{3}$$

respectively.

In order to close the system of equations, an expression for the rate of mass transfer between the liquid and the vapour has to be introduced. In the approach proposed by Sauer and Schnerr this is done by considering the equation of motion of a single bubble of radius R and rearranging it to the following form:

$$\dot{m} = \frac{\rho_l \rho_v}{\rho}(1-\alpha)\frac{3}{R}\sqrt{\frac{\frac{2}{3}(p-p_v)}{\rho_l}}. \tag{4}$$

2.2 Ffowcs-Williams Hawkings Analogy Implementation

Ffowcs-Williams Hawkings acoustic analogy extends the Lighthills equation to predict noise originating from the presence of a turbulent flow (Ffowcs Williams & Hawkings 1969). Based on rearranging the mass and momentum conservation equations of the fluid, a solution to the inhomogeneous wave equation is introduced as

$$p'(\boldsymbol{x},t) = p'_T(\boldsymbol{x},t) + p'_L(\boldsymbol{x},t) + p'_Q(\boldsymbol{x},t), \tag{5}$$

where $\boldsymbol{x}$ and t are the receiver position and time, respectively, p' is the acoustic pressure disturbance, and subscripts T, L and Q refer to the thickness (monopole), loading (dipole) and quadrupole (non-linear) contributions (Lyrintzis 2002, Ianniello et al. 2012). Each of the terms on the right-hand-side of Equation (5) is computed by evaluating a surface integral of quantities dependent on the state of the flow. Note that the when a porous formulation is used, as is the case in the present work, the non-linear term for sources located within the control surface are accounted for via the thickness and loading contributions. This also implies that for such a formulation the monopole and dipole contributions lose their physical meaning (Ianniello et al. 2012). In the present approach the non-linear contribution from noise sources located outside the integration surface (IS) is ignored based on the assumption that the IS extends far enough to encompass all relevant sources. This assumption may be expected to be challenged in the wake region where the accelerated flow induced by the propeller penetrates the control surface. Due to the inherent dissipation involved in using an URANS approach, however, it is expected that vortical structures will have lost their coherence by the time the reach the downstream IS extent and therefore will not generate any spurious noise which would otherwise have to be accounted for by solving a volume integral for the $p'_Q(\boldsymbol{x},t)$ term outside the control surface.

FWH analogy makes use of two intermediate variables, U_i and L_i. For incompressible flow one may neglect the density disturbance. Moreover, when the control surface is stationary the expressions for the acoustic variables may be simplified even further, yielding

$$U_i = u_i,$$
$$L_i = (p - p_0)\hat{n}_j + \rho_0 u_i (u_i \cdot \hat{n}_i). \quad (6)$$

In Equations (8) u_i is the fluid velocity at a point, $\hat{n}$ is a unit vector normal to the control surface, p is the local fluid pressure, p_0 is the reference pressure level, and ρ_0 is the reference fluid density.

For a stationary control surface S, the FWH Formulation 2 thickness and loading terms may be computed using

$$4\pi p_T'(\boldsymbol{x}, t) = \int_S \left[\frac{\rho_0 \dot{U}_n}{r}\right]_\tau dS, \quad (7)$$

and

$$4\pi p_L'(\boldsymbol{x}, t) = \frac{1}{c_0}\int_S \left[\frac{\dot{L}_r}{r}\right]_\tau dS + \int_S \left[\frac{L_r}{r^2}\right]_\tau dS. \quad (8)$$

Here c_0 denotes the speed of sound in the medium, r is the radiation direction, dot defines a source time derivative, and subscripts r and n refer to the dot product of the quantity in question with a unit vector in either radiation or normal directions, respectively.

Invoking the incompressible flow assumption renders the fluid dynamic part of the solution significantly less computationally intensive. It does, however, imply that only the low-frequency part of noise associated with blade-pass frequency may be modelled as no other perturbations will be present in the CFD solution. One may think of the FW-H as a transfer function which translates the fluid dynamic data into their acoustic representation. Simplifying the former affects the latter.

In order to account for the fact that the sound contribution of an infinitesimal control surface element will take a finite amount of time to travel between the source and the receiver all of the quantities in Equations (7) and (8) must be evaluated at an appropriate emission time, τ,

$$\nabla = \tau + \frac{\boldsymbol{x} - \boldsymbol{y}}{c_0}, \quad (9)$$

where $\boldsymbol{y}$ is the location of the source (integration surface element). In the current implementation of the FWH, developed for the purpose of the discussed project, the control surface is defined by a set of cell faces. This provides less control over the density and shape of the control surface than if the flow field was interpolated onto an independent discreet surface. On the other hand, the used approach introduces no additional errors and avoids local pressure and velocity perturbations from being lost.

2.3 Governing Flow Equations

Unsteady RANS is used in order to model the flow around a rotating propeller. While this method does not allow for broadband noise to be computed, the tonal component of the noise signature may still be captured (Ianiello et al. 2013). It was therefore deemed beneficial to use this modelling approach, taking the advantage of less stringent grid requirements and shorter computational times when compared with LES, given the preliminary nature of the investigation.

The incompressible, Reynolds Averaged Navier-Stokes equation for a velocity field $\boldsymbol{U}$ and a pressure field p is

$$\frac{\partial \overline{\boldsymbol{U}}}{\partial t} + \nabla \cdot (\overline{\boldsymbol{U}} \otimes \overline{\boldsymbol{U}}) = -\frac{1}{\rho}\nabla \bar{p} + \nu \nabla^2 \overline{\boldsymbol{U}} - \nabla \cdot \boldsymbol{\tau}, \quad (10)$$

where ν is the kinematic viscosity, ρ denotes the fluid density and $\boldsymbol{\tau}$ is the Reynolds stress tensor. The conservation of mass is described by the continuity equation,

$$\nabla \cdot \overline{\boldsymbol{U}} = 0. \quad (11)$$

In order to close eq. (10) an expression is needed for the non-linear stress term. This is achieved by assuming that the Reynolds stress may be related to the mean velocity gradients. This allows the effect of the local velocity and pressure fluctuations on the mean flow to be computed using an assumed turbulent viscosity field. k-ω SST model is used to provide an expression for turbulent viscosity, as described by Menter (1994).

3 CASE STUDY

3.1 Overview

Table 1 shows the particulars of the considered Potsdam Propeller Test case in cavitating scenario 2.3.1, as describe by Abdel-Maksoud (2011). This controllable pitch propeller has established itself as a well know test case for marine computational fluid dynamics (CFD) validation and was therefore deemed suitable for the purpose of this study. It should be mentioned that, to the authors' knowledge, no openly available noise measurements exist for this geometry and so any future validation will have to rely on analytical models and comparing against other numerical solutions.

Table 1: Parameters of the Potsdam Propeller test case in cavitation scenario 2.3.1 (Abdel-Maksoud 2011).

Radius [m]	0.125	Eff. Area ratio	0.779
P/D	1.567	c at 70% R [mm]	106.35
No. blades	5	m at 70% R [mm]	3.09
rpm	1500	σ (rps-based)	2.024
J	1.019	Blade-pass freq. [Hz]	125

3.2 Mesh and Boundary Treatment

The numerical domain, shown in Figure 1, extends 10 diameters in the downstream, and 5D in the radial and upstream directions. In total, 6 million hexahedral, unstructured cells created using the OpenFOAM snappyHexMesh utility were used to discretise the domain. Over 3 million of the elements were located in the propeller boundary layer and the sliding mesh region, shown in red in Figure 1. Cell size inside the latter was kept constant in order to reduce the dispersion and dissipation errors, although at an increased computational cost. Additional volumetric refinement was also applied in the regions where tip vortices were expected to improve the resolution of the associated cavities. In order to enable mesh motion, interpolation was performed between the stator and the rotor zones using an Arbitrary Mesh Interface (AMI) available in OpenFOAM. Relatively large size of the domain and coarse mesh elements close to the external boundaries were used in order to reduce the amount of reflections travelling back into the domain.

To better understand the effect of the importance of an appropriate definition of the FWH integration surface, three control surfaces were used: the inner and outer sides of the sliding mesh interface and a rectangular box, shown in red and orange in Figure 1, respectively, and henceforth referred to as inner cylinder, outer cylinder, and box surfaces, respectively.

Table 2 shows the locations of a total of 11 receivers which were placed around the propeller. These were distributed at a distance of 100 m along a half-circle spanning between the two ends of the shaft centreline in the x-y plane. This arrangement aimed to provide information about directivity of the radiated sound.

Fixed velocity and turbulence inlet was chosen to simulate uniform inflow conditions. Ambient pressure required to achieve the desired cavitation number was imposed using a fixed pressure value at the outlet. The outer walls were assumed to be slip, while no-slip condition was applied to the propeller, hub, and shaft. To reduce the computational effort wall-functions were used on the no-slip boundaries. To match the experimental conditions the water and vapour were assigned densities of 997.44 and 0.023 kg m^{-3}, respectively, and kinematic viscosities of $9.337 \cdot 10^{-7}$ and $4.273 \cdot 10^{-6}$ kg m^{-2}, respectively. The saturation pressure was taken to be 2818 Pa.

First order time discretisation was used, and the convection term of the RANS equation was resolved using first-second order scheme. First order schemes were used to model the turbulent quantities and van Leer scheme with interface compression was applied to the volume fraction field.

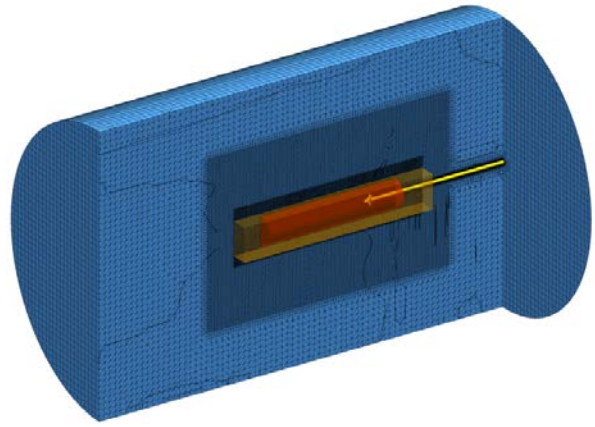

Figure 1: Overview of the computational domain, grid refinement regions and the placement of the cylindrical (red) and rectangular (orange) FWH integration surfaces.

4 RESULTS AND DISCUSSION

4.1 Cavitation Characteristics

Figures 2 and 3 show the predicted and experimentally observed cavity extents, respectively. The simulated results show a similar pattern with significant amount of tip cavitation, accompanied by an attached root cavity. Noticeably, however, the predicted extent of cavitation is under predicted with respect to the observed data. It is also interesting to note that due to the use of additional refinement in wake of the blade tips the vortex structure in that region is well resolved despite the fact that RANS is used to model the flow. This allows for the tip vortex cavity to extend approximately half of the mean chord length downstream before disappearing. The tip vortex structure may be seen to end abruptly as the associated refinement region ends, indicating one of the limitations of the numerical grid used.

Table 2: Locations of the receivers placed around the propeller along a semi-circular arc in the x-y plane.

No.	Elevation [deg]	x [m]	y [m]
0	0	-100.0	0.0
1	18	-95.1	30.9
2	36	-80.9	58.8
3	54	-58.8	80.9
4	72	-30.9	95.1
5	90	0.0	100.0
6	108	30.9	95.1
7	126	58.8	80.9
8	144	80.9	58.8
9	162	95.1	30.9
10	180	100.0	0.0

Figure 2: View of the predicted cavitation extent (blue, $\alpha = 0.5$) and the computed tip and root vortices (orange, $\omega = 1500\ s^{-1}$).

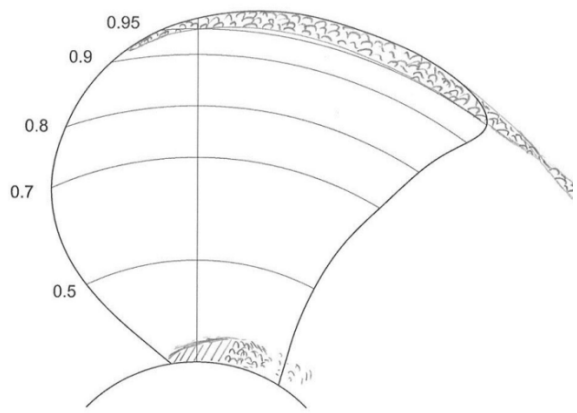

Figure 3: Sketch of the experimentally observed cavitation extent for the Potsdam Propeller case 2.3.1 (Abdel-Maksoud 2011).

Figure 4 presents the power spectral density function of the total cavity volume in the domain. No peak may be seen in the data around the blade pass frequency of 125 Hz. Second and fourth harmonics, however, show distinguishable peaks. These are of small magnitude and correspond to variations of less than ±10%, making it difficult for them to be seen by analysing the time trace or visualising the evolution of the cavity extents. This indicates a well-known issue of URANS simulations predicting unphysically steady cavities, which is discussed for instance by Wikstrom (2006). This behaviour could be further encouraged by the use of a coarse mesh and steady inflow conditions. It is also possible that due to the integral nature of the total cavity volume small fluctuations occurring simultaneously on five blades of the propeller could not make themselves visible in the spectrum over the sampling period. Nonetheless, this indicates the importance of using higher fidelity turbulence modelling techniques, such as DES or LES, or more advanced cavitation models adapted to be used with URANS if the broadband noise component induced by cavitation is to be studied.

4.2 Propeller Loading

Table 3 presents the mean torque and thrust computed in the non-cavitating condition, used to initialise the discussed simulation, and their comparison with the experimentally measured values for this advance coefficient. These are defined for advance ratio,

$$J = \frac{V_r}{nD} = \frac{V_a + 0.7\omega R}{2nR}, \tag{12}$$

as

$$K_T = \frac{T}{\rho n^2 D^4}, \tag{13}$$

$$K_Q = \frac{Q}{\rho n^2 D^5}. \tag{14}$$

In Equations (12-14) $V_a$is the advance velocity, ω is the rotational velocity, n is the number of revolutions per second, R is the propeller radius, and T and Q denote mean torque and thrust, respectively. Good agreement has been achieved, despite the fact that a wall model and a relatively coarse mesh were used.

Figure 5 depicts the power spectral density function of the thrust produced by each blade of the propeller. As the inflow is steady there is no dependence in the signal on the multiples of blade-rate frequency. Furthermore, as URANS is used no broadband components are present and instead a steady drop-off with frequency is seen in the data, as expected. This emphasises the need of using more advanced turbulence modelling techniques or correcting the Lighthill stress tensor based on the Boussinesq hypothesis, as described by Ianiello et al. (2012), if the noise due to turbulence is to be considered. As already mentioned, the FWH implementation used herein is aimed to be used primarily with Large Eddy Simulations and so no correction was applied.

Table 3: Predicted thrust and torque in compared to the experimental results for the non-cavitating condition (CFD data averaged over 5 revolutions).

EFD	Kt	0.3910
	10 Kq	0.9604
CFD	Kt	0.3923
	10 Kq	1.0050
	ϵ Kt	0.32%
	ϵ 10 Kq	4.64%

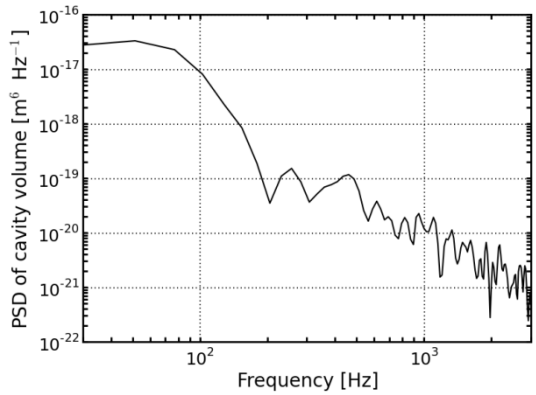

Figure 4: Power spectral density function of the total cavity volume extent for a threshold value of $\alpha \leq 0.95$.

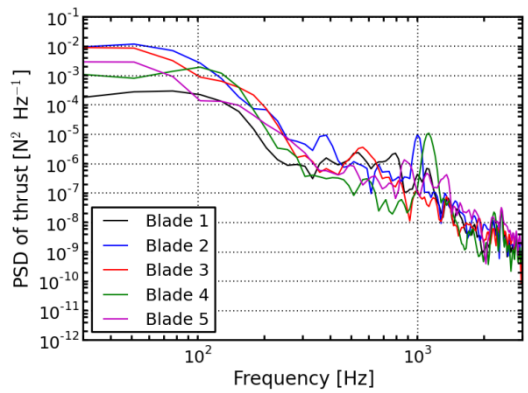

Figure 5: Power spectral density function of the thrust produced by each of the propeller blades.

4.2 Radiated Noise Signals

Figure 6 shows a time trace of acoustic pressure for receiver located downstream and above the propeller (receiver 4) computed using the box integration surface and with components above 500 Hz filtered out. The data presented shows the tonal character of the predicted signal, with peaks occurring over a period of approximately one-fifth of a revolution.

Data in Figure 7 shows acoustic disturbance for 5 receivers computed using the box surface over a period of 1/5th of a revolution. Again, one may note that all receivers show peaks corresponding to the passing time of the blades. Another noteworthy observation are the marginally larger magnitudes of receiver pressure recorded for listeners closer to the shaft line (7 and 9). This indicates a dipole character of the dominant noise source, likely associated with the loading component. The noise signal of the receiver facing the wake of the propeller may be seen to diverge from the tonal character of the noise experienced by other receivers.

Data in Figure 8, showing root mean square value of the receiver pressure computed using the box integration surface, confirms the dipole character of the acoustic source created by the propeller. The fact that the RMS does not tend to zero at the propeller plane and that there is a sizeable contribution of the thickness FWH term does indicate the presence of a monopole source alongside the dominant dipole. This may be likely associated with the presence of the cavities or the thickness noise induced by the blades. The dipole FWH term may be seen to be asymmetric about the propeller plane, causing the overall directivity pattern to show higher noise values for the downstream receivers. This indicates, firstly, that the nature of the FWH terms may lose its physical meaning when the porous formulation is used Lyrintzis (2002), as evident from the dipole term not representing a perfect dipole source. Furthermore, this observation suggests the presence of additional noise source in the wake of the propeller, which may be attributed to large velocity gradients in this region (Ianiello et al. 2013). As shown by said authors, explicitly computing the volume integral of the non-linear FW-H term for the turbulent velocities may improve the behaviour in this region. Finally, the observed asymmetry of the noise directivity may have been caused by noise sources occurring on and outside of the control surface as the wake passes through the control surface. When an open control surface was used even larger discrepancies were observed.

4.3 Radiated Noise Spectral Characteristics

Figure 9 presents harmonics of the acoustic pressure computed with the box integration surface for receiver 4. The first harmonic, as expected, has a dominant effect. Higher blade pass harmonics have a progressively smaller effect. Analysis of even higher frequencies revealed no high frequency dependence. This behaviour was expected given that RANS was used to solve the flow, thus disallowing broadband turbulent noise to be captured, and since the only noticeable oscillations of the cavity volume were observed around the second harmonic of the blade pass frequency.

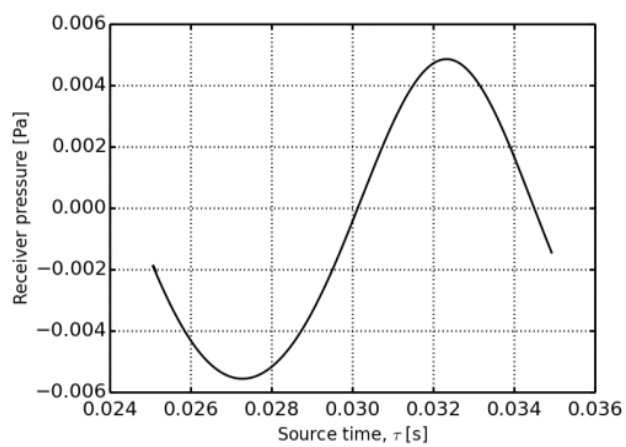

Figure 6: Predicted acoustic pressure disturbance at receiver 4 computed using the rectangular box surface (low-pass filtered at 500 Hz).

4.4 FWH Term Distribution

Figure 10 shows the contribution of each of the control surface faces to the sound pressure level computed at receiver 10 using the box and external cylinder surfaces at a snapshot in time. The data presented is divided by the area of each face in order to allow more direct comparison between surfaces of different mesh densities. Also, the scale has been saturated at the extrema to better illustrate the contribution of the wake structures. Comparing the two figures shows that due to them being separated by approximately 1.5 propeller diameters in space there is a phase difference between the predicted signals. Moreover, the cylindrical surface may be seen to deliver higher contribution per unit area, explaining the difference in predicted sound pressure levels observed in Figure 9. It is also interesting to note the periodic character of the wake structure contributions, tying-in with the conclusions drawn from examining Figure 8 about the velocity gradients in this region contributing to the predicted noise.

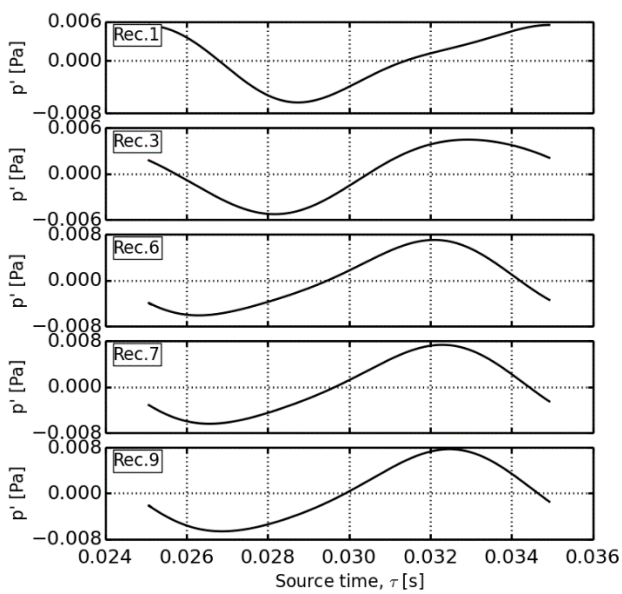

Figure 7: Time traces of acoustic pressure for 6 receivers computed using the box integration surface.

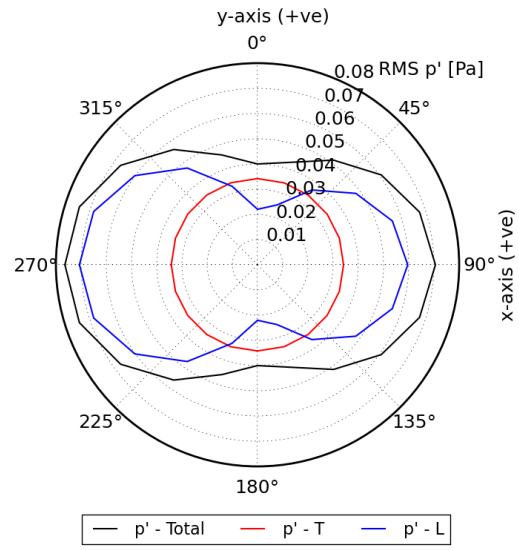

Figure 8: Radial distribution of the root mean square value of the receiver pressure for the box surface (data on the –ve side of y-axis mirrored).

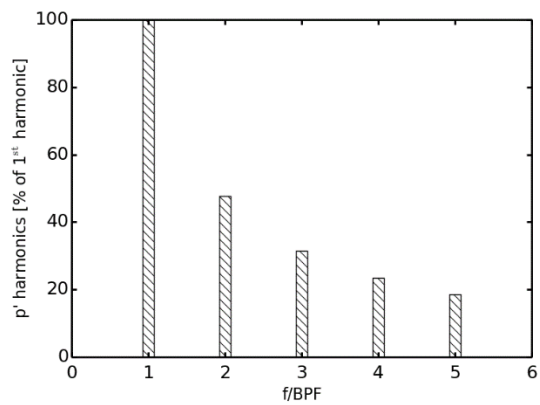

Figure 9: Blade harmonics of the acoustic disturbance at receiver 4 as a fraction of the first harmonic.

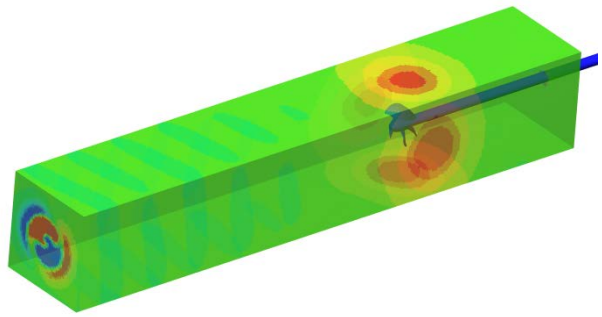

(a)

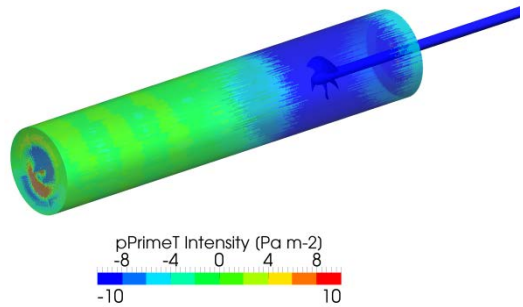

(b)

Figure 10: Contribution of each of the box **(a)** and external cylinder **(b)** integration surface elements to the acoustic pressure for receiver 10. Data divided by face area of each element, scale saturated at the extrema to show the effect of the wake structures.

5 CONCLUSIONS AND FUTURE WORK

The use of porous Ffowcs-Williams Hawkings analogy together with a mass transfer cavitation model by Sauer & Schnerr coupled to an unsteady RANS simulation has been demonstrated to be a viable tool for marine propeller noise assessment. The presented results indicated the presence of a strong dipole source related to the blade pass frequency, as well as the occurrence of a monopole source, likely associated with the cavity volume variations and/or the effect of blade thickness. A noticeable contribution of the velocity gradients present in the wake to the sound predicted has also been observed.

In the presented form the methodology suffered from under predicted unsteady behaviour of the cavities and the fact that the broadband noise spectrum generated by turbulence was unaccounted for. This indicated a substantial disadvantage of using unsteady RANS computations in the hydroacoustic context. While certain modelling paths may be taken to mitigate this limitation, both in terms of cavitation and noise modelling, the use of more advanced turbulence modelling techniques, such as DES or LES, may prove vital if more in-depth studies are to be undertaken.

Furthermore, a significant dependence of the predicted noise on the handling of the downstream control surface extent has been seen. One of the primary disadvantages of the approach used is the need to balance the grid requirements against the will to account for noise radiated by large control volumes. The distribution of the noise terms on the side of the control surface intersecting the wake has shown to contribute significantly to the radiated noise signal, which may or may not be physically correct. Further studies involving open-ended surfaces are therefore planned to further explore this issue.

In conclusion, the presented methodology may prove a useful tool for hydroacoustic characterisation of commercial ship propellers if such design calculations will become required by the international or classification society regulations. Further work is needed in making it more reliable, however, predominantly in being able to account for the broadband part of the acoustic signature and in proving that the results produced are robust enough to stand up to the requirements of everyday use in a commercial environment.

ACKNOWLEDGMENTS

The authors would like to acknowledge the use of OpenFOAM® libraries and the Iridis 4 supercomputer of the University of Southampton for all of the presented simulations.

REFERENCES

Abdel-Maksoud, M. (ed) (2011), Proceedings of the Workshop on Cavitation and Propeller Performance, Second International Symposium on Marine Propulsors - SMP'11, 17 – 18 June, Hamburg, Germany

Bensow, R. (2011), Simulation of the unsteady cavitation on the Delft Twist11 foil using RANS, DES and LES, in: 2nd International Symposium on Marine Propulsors, no. June, Hamburg, Germany

Brennen, C. E. (1993). Cavitation bubble dynamics and noise production, in: 6th International Workshop on Multiphase Flow, Tokyo, Japan

Brentner K. S. & Farassat F. (1998), An analytical comparison of the acoustic analogy and Kirchhoff formulation for moving surfaces, AIAA Journal, Vol. 36 (8), pp. 1–17

Ffowcs Williams, J. & Hawkings, D. L. (1969), Sound generation by turbulence and surfaces in arbitrary Motion, Philosophical Transactions of the Royal Society of London Series A, Mathematical and Physical Sciences, vol. 264, no. 1151, pp. 321–342

Hildebrand, J. (2009), Anthropogenic and natural sources of ambient noise in the ocean, Marine Ecology Progress Series, vol. 395, pp. 5–20

Hsiao, C.-T., & Chahine, G. (2004), Prediction of tip vortex cavitation inception using coupled spherical and

nonspherical bubble models and Navier-Stokes computations, Journal of Marine Science and Technology, vol. 8(3), pp. 99–108

Ianniello, S., Muscari, R., and Mascio, A. D. (2012), Hydroacoustic characterization of a marine propeller through the acoustic analogy, Sustainable Maritime Transportation and Exploitation of Sea Resources, pp. 991–1000

Ianiello, S., Muscari, R., Di Mascio, A. (2013), Ship underwater noise assessment by the acoustic analogy. Part I: nonlinear analysis of a marine propeller in a uniform flow, Journal of Marine Science Technology, vol. 18, pp. 547-570, doi: 10.1007/s00773-013-0227-0

Jamaluddin, A. R., Ball, G. J., Turangan, C. K., Leighton, T. G. (2011), The collapse of single bubbles and approximation of the far-field acoustic emissions for cavitation induced by shock wave lithotripsy, Journal of Fluid Mechanics, vol. 677, pp. 305–341

Kellet, P., Turan, O., Incecik, A., Underwater Noise and Marine Wildlife: Current and Future Implication and Assessment, in: A. Yucel Odabasi Colloquium Series, 6th-7th November, Istanbul, Turkey, 2014, pp. 63–69.

Kirsteins, I., Clark, P., Atlas, L. (2011), Maximum-likelihood estimation of propeller noise modulation characteristics, Underwater Acoustic Measurements: Technologies and Results

Lloyd, T. P. (2013), Large eddy simulations of inflow turbulence noise: application to tidal turbines, PhD Thesis, University of Southampton

Lloyd T. P., Rijpkema D., Van Wijngaarden E. (2014), Implementing the Ffowcs Williams-Hawkings acoustic analogy into a viscous CFD solver, in: 17th Numerical Towing Tank Symposium (NuTTS), 28-3s0th September, Marstrand, Sweden

Lyrintzis, A. S. (2002), Surface Integral Methods in Computational Aeroacoustics - From the CFD Near-Field to the Acoustic Far-Field, CEAS Workshop ”From CFD to CAA”, (Athens, Greece), pp. 1–53

Marte, J. E. & Kurtz, D. W. (1970). A review of aerodynamic noise from propellers, rotors and lift fans. NASA Technical Report 32-1462, Jet Propulsion Laboratory, Caltech, Pasadena, California

Menter, F. R. (1994). Two-equation eddy-viscosity turbulence models for engineering applications. AIAA Journal, Vol. 32, No.8, pp. 1598-1605. doi: 10.2514/3.12149

Park, C., Seol, H., Kim, K., Seong, W. (2009), A study on propeller noise source localization in a cavitation tunnel, Ocean Engineering, vol. 36, pp. 754–762

Plesset, M. S. & Prosperetti, A. (1977), Bubble dynamics and cavitation, Annual Review of Fluid Mechanics

Salvatore, F. & Ianniello, S. (2002), Preliminary results on acoustic modelling of cavitating propellers, IABEM 2002, International Association for Boundary Element Methods, UT Austin, TX, USA

Sauer, J. & Schnerr, G. H. (2001), Development of a new cavitation model based on bubble dynamics, Zeitschrift fur Angewandte Mathematik und Mechanik, vol. 81, pp. 561–562

Seol, H., Suh, J.-C., Lee, S. (2005), Development of hybrid method for the prediction of underwater propeller noise, Journal of Sound and Vibration, vol. 288, pp. 345–360

Urick, R. J. (1984), Ambient Noise in the Sea, Undersea Warfare Technology Office, Naval Sea Systems Command, Dept. of the Navy, Washington D.C.

Woo Shin, K. (2010), Cavitation simulation on marine propellers, PhD thesis, Technical University of Denmark

Wikstrom M. (2006). Approaching large eddy simulation of cavitating flows for marine applications, Ph.D. thesis, Chalmers University of Technology